# Simulation of Electromagnetic Inductive Drive for Liner Implosion Fusion Thruster System Using Filamentary Approaches

**IEPC-2017-506**

*Presented at the 35th International Electric Propulsion Conference*
*Georgia Institute of Technology – Atlanta, Georgia – USA*
*October 8–12, 2017*

Akihisa Shimazu*
*University of Washington, Seattle, WA, 98195, USA*

*and*
John Slough†
*MSNW LLC, Redmond, WA, 98052, USA*

**Abstract: A liner implosion based fusion thruster concept is a pulsed fusion-electric hybrid propulsion system, which offers unique capability to over come the typical power limitation in the electrical propulsion device. In this system, fusion energy is produced by an inductively driven metal liner compression of a Field Reversed Configuration (FRC) plasmoid. The key to understanding the performance of the liner implosion based fusion thruster is an accurate understanding of the inductively driven liner behavior that governs the efficiency of the FRC capture and fusion reactions. In order to better characterize the liner behavior during implosion, we have implemented an axisymmetric and fully 2-dimensional model for the liner and the inductive drive. This model is based on a sequential coupling of a well-known filamentary modeling technique for electromagnetism and explicit large strain finite element modeling technique for structural mechanics. The thermal model is also coupled using the locally adiabatic assumption for the temperature dependent resistivity. The model is used to perform a preliminary analysis of a liner implosion for the conditions suitable for the liner implosion fusion thruster system. A comparison is made with the previous pseudo-1D liner model to assess the importance of the 2D effects for the liner performance. It was seen that the new model predicts reduced energy transfer efficiency to the liner and is more dissipative compared with the previous model.**

## Nomenclature

$A$ = magnetic vector potential
$B$ = magnetic field
$C$ = capacitance
$E_t$ = tangent modulus
$F$ = deformation gradient
$G$ = axisymmetric magnetostatic Green's function
$H, N$ = shape function
$I$ = current
$J$ = current density
$K$ = bulk modulus
$L$ = inductance

*Graduate Research Assistant, William E. Boeing Department of Aeronautics & Astronautics, akihis2@uw.edu
†President and Director of Research, sloughj@msnwllc.com

$M$ = mutual inductance
$R$ = resistance
$S$ = cross-section area
$T$ = temperature
$V$ = voltage
$\mathcal{V}$ = volume
$b$ = elastic finger tensor
$c_{sp}$ = specific heat
$e$ = Euler-Almansi strain tensor
$f$ = relative deformation gradient
$m$ = mass
$p$ = pressure
$r, z, \phi$ = cylindrical coordinates
$s$ = deviatoric Kirchhoff stress
$u$ = displacement
$\alpha_p$ = plastic correction factor
$\alpha_r$ = temperature coefficient for resistivity
$\epsilon$ = infinitesimal strain
$\mu$ = shear modulus
$\mu_0$ = permeability of free space
$\lambda$ = relative azimuthal stretch
$\xi, \eta, \zeta$ = local coordinates
$\rho$ = resistivity
$\rho_m$ = mass density
$\sigma_y$ = yield strength
$\tau$ = Kirchhoff stress

# I. Introduction

One of the greatest obstacle in the ability to extend the reach of a human space exploration is the lack of a suitable propulsion system which enables rapid transportation of massive cargoes necessary for manned missions. For missions outside of Earth's sphere of influence, a long mission time required by today's chemical and electrical propulsion system increases the associated risks such as health and political issues; health issues associated with zero-g and prolonged radiation exposures increases the risk for the astronauts, and political issues associated with retaining public interest and governmental support may make such mission impossible from funding perspectives. A long mission time also requires durable and fail proof environmental control and life support system, adding mass and cost to the mission. Furthermore, due to the added mass from all of these systems, the total mass required for the mission may exceed the present launch capability, causing mission to require multiple launches, in-space assembly, and space rendezvous, adding complexity and further cost to a mission.

One possible propulsion system which enables rapid transportation of massive cargoes is a pulsed fusion-electric hybrid propulsion system, where the energy limitation of typical electric propulsion devices is overcome by a supplemental fusion energy produced from the fusion reaction. One possible method to obtain fusion-electric hybrid system is to use electromagnetically imploded cylindrical metal shells (liners) to compress a Field Reversed Configuration (FRC) plasmoid into a fusion configuration and convert the resulting energy from the electromagnetic implosion and the fusion energy directly into thrust. The liner is utilized as both a driver for the fusion reaction and a thruster propellant. Thus, the thrust is obtained from both the fusion energy produced by the FRC and the electromagnetically generated kinetic energy of the liner, offering hybrid performance of the two systems. Due to the additional energy of the fusion reaction, significant thrust can be obtained compared with typical electric propulsion device. The presence of electric energy produced from solar panels allows the thruster to operate in pulsed mode, where it relaxes the confinement requirement of the fusion process and removes the requirement of complex energy recovery scheme from the fusion reaction.

A conceptual propulsion system based on the liner implosion fusion concept has been developed by

MSNW LLC, and it is called the Fusion Driven Rocket (FDR).[1] In the pulsed operation of the FDR, first, a capacitor bank system is charged to the operating voltage using solar panels. Once the capacitor bank is ready, the electromagnetic inductive drive is fired, and it independently drives thin metal liners into radial implosion and axial translation. The liner is translated axially towards the thruster throat for capturing and compressing the FRC at the throat exit. The inductive drive also shapes the liner implosion for a maximum compression efficiency of the FRC target, as well as to bias the blast exhaust to axially exit the thruster for minimizing the back fire of the implosion fragments. In a separate formation system, an FRC is formed using fusion propellants, and then translated axially to inject itself into a converging metal liner at the thruster throat. The injected FRC is captured by the liner, and the inertia of the imploding liner compresses the captured FRC to fusion conditions in the thruster nozzle. The fused FRC releases fusion energy and expands, which in turn heats and vaporizes the metal liner in the magnetically insulated nozzle. The resulting plasma-metal mixture is rapidly expanded in the nozzle and is exhausted to produce thrust. This cycle is repeated to continuously generate thrust.

Since the liner convergence and the FRC capture occurs in the nozzle region of the thruster, away from the electromagnetic inductive drive system and the FRC formation system, only the thruster nozzle is affected by the fusion event. As such, the thruster nozzle is magnetically insulated to avoid highly charged thruster exhaust from striking the nozzle walls. The metal liners also serve to buffer the spacecraft against radiant, neutron, and particle energy from the plasma, which further isolates the spacecraft and the thruster driver system from the fusion process. Thus crucial and sensitive components are shielded away from the fusion event by the natural construction of the thruster system.

In the previous system design of the FDR thruster system, it was found that the kinetic energy that is transferred to the liner through the electromagnetic inductive drive is the biggest driver in the performance of the thruster system to the first order.[2] Thus, a subsequent work focused on exploring the favorable design space for the electromagnetic inductive drive, using a pseudo-1D liner model, which tried to identify the liner performance as a function of capacitor bank circuit configurations.[3] However, while the previous pseudo-1D model was successful in characterizing the driver circuit dependence on the liner implosion behavior, it could not resolve 2D effects such as barrel distortion of the liner due to the edge effect. Furthermore, the ability to shape and axially translate the liner could not be modeled in the 1D frame work, and they were ignored.

In order to overcome the limitation of the pseudo-1D liner model, an improved 2-dimensional model is developed, which addresses the shortcoming of the previous model. In particular, fully 2-dimension behavior of electromagnetism, structural mechanics, and thermal physics are accounted to ensure that the 2-D effects of the liner can be captured. A well-known filamentary modeling technique is used to model the driver coil and the liner to obtain a full 2-dimensional behavior of the magnetic fields and the current distribution. A 2-dimensional large strain structural model is coupled with the filamentary model to obtain the time-dependent dynamics of the liner implosion. The thermal heating caused by the Joule heating is modeled using a locally adiabatic assumption, with thermal-structural couplings neglected.

This paper is organized as follows. In section II, a complete description of the 2-dimensional filamentary model implemented for the modeling of the electromagnetic inductive drive and the liner is given. In section III, a preliminary results obtained from the model discussed in section II is presented. Finally, in conclusions, future plans for improve this model is briefly presented.

## II. Filamentary Modeling of Electromagnetic Inductive Drive

In order to model the electromagnetic inductive drive and the imploding liner, a well-known filamentary modeling approach is used to obtain a full 2-dimensional behavior of the magnetic fields and the current distributions. In the filamentary modeling approach, coils for the inductive driver and the liner are discretized into axisymmetric current carrying rings with an uniform current density, or filaments. Filaments are inductively coupled together, and circuit equations are used to couple filaments to the driver circuit. A dynamic structural and thermal model can be coupled to the filamentary circuit model to obtain a fully dynamic behavior of the inductive driver and the liner system.

The filamentary modeling technique was first successfully applied to the inductively driven electromagnetic flux compression technique by Miura and Nakao.[4] An improved modeling approach was suggested and successfully implemented by Novac and the group at Loughborough University in U.K., which improved electromagnetic load calculation and structural dynamics.[5] In this present model, for the calculation of the current distribution in the filaments, a similar approach as the previous two models is used. However,

important improvements are made to the filamentary model to generalized the model, and couple a fully 2-dimensional structural model to the filamentary circuit model. In this section, a detailed description of the numerical code used to model the electromagnetic inductive drive is given.

### A. Filamentary Circuit Equations

To calculate the current distribution in the driver system and the liner, the cross-sections of coils (including the liner) are divided into a mesh of small triangles. Given that there are $N_p$ total number of coils with the $\alpha$-th coil divided into $N_e^\alpha$ filamentary elements, the filamentary circuit equation for the $i$-th filament in the $\alpha$-th coil can be written to be

$$\sum_{\beta=1}^{N_p}\sum_{j=1}^{N_e^\beta}\left[M_{ij}^{\alpha\beta}\frac{dI_j^\beta}{dt}+\frac{\partial M_{ij}^{\alpha\beta}}{dt}I_j^\beta+\frac{1}{\mathcal{V}_i^\alpha}\frac{d\mathcal{V}_i^\alpha}{dt}M_{ij}^{\alpha\beta}I_j^\beta\right]+R_i^\alpha I_i^\alpha=V^\alpha(t), \tag{1}$$

where $M_{ij}^{\alpha\beta}$ is a mutual inductance between the $i$-th filament in the coil $\alpha$ and the $j$-th filament in the coil $\beta$, $I_j^\beta$ is the current through the $j$-th filament in the coil $\beta$, $\mathcal{V}_i^\alpha$ is the volume of the $i$-th filament in the coil $\alpha$, $R_i^\alpha$ is the resistance of the $i$-th filament in the coil $\alpha$, $I_i^\alpha$ is a current through the $i$-th filament in the coil $\alpha$, and $V^\alpha(t)$ is the time dependent voltage applied to the coil $\alpha$.

In the Eq. 1, $V^\alpha(t)=0$ for typical liners that are not connected to any external circuits, and $\partial M_{ij}^{\alpha\alpha}/\partial t=0$ for typical case when the driver coils has negligible dynamic coil movements. The Eq. 1 describes the full current evolution characteristic of the filamentary driver and liner system, given initial conditions and description of the mutual inductances, resistances, and the applied circuit voltage. Due to the system current being described completely by Eq. 1, the full magnetic field distribution within the filamentary system is also fully characterized by the same equation.

The resistance of the $i$-th filament is defined to be

$$R_i=\frac{2\pi\bar{r}_i\rho}{S_i} \tag{2}$$

where $\bar{r}_i$ and $S_i$ is the mean radius and the cross-section area, respectively, of the $i$-th filament. The mutual inductance between the two filaments is defined to be

$$M_{ij}=\frac{\mu_0}{2}\frac{1}{S_iS_j}\iiiint G(r,z;r',z')\,dr'dz'drdz, \tag{3}$$

where $\mu_0$ is permeability of free space, $S_i$ and $S_j$ are the cross-section area of the $i$-th and $j$-th filament, respectively, and $G(r,z;r'z')$ is an axisymmetric magnetostatics Green's function defined as

$$G(r,z;r'z')=\sqrt{(r+r')^2+(z-z')^2}\left[(2-k^2)K(k)-2E(k)\right],$$

where $K(k)$ and $E(k)$ are the complete elliptic integral of the first and second kind, respectively, and the modulus $k$ is defined to be

$$k^2=\frac{4rr'}{(r+r')^2+(z-z')^2}.$$

The quadruple integral in Eq. 3 is over the two areas of the filamentary elements, and the un-primed and the primed variables are associated with the $i$-th and the $j$-th filament, respectively. It can be seen that the mutual inductance of filamentary elements is simply proportional to the area averages of the Green's function. The detailed derivation of the filamentary circuit equations and various circuit quantities are given in Appendix A.

In theory, the Eq. 3 can be numerically integrated over the two filamentary triangle elements to any arbitrary precision. However, exact numerical integration can be computationally expensive as the integral must be calculated every time the system geometry is updated. To reduce computational cost, the integral can be approximated using Gaussian quadrature to simplify the mutual inductance calculation. We note that the Green's function in Eq. 3 blows up when Gaussian quadrature points for the un-primed and primed coordinate overlaps with each other. This condition may be encountered for the case of the self-inductance calculation or the mutual inductance calculation of the neighboring filaments, if poor choice of Gaussian quadrature points are made. Thus, a symmetric Gaussian quadrature of degree 2 for standard triangle is

used to take advantage of the non-uniqueness of the Gaussian quadrature points for this case. We ensure that the un-primed and primed coordinates choose a different set of second degree Gaussian quadrature points to force no overlap. With this, the approximate mutual inductance between the $i$-th and the $j$-th filamentis given to be

$$M_{ij} \approx \frac{\mu_0}{36} \sum_{i=1}^{3} \sum_{j=1}^{3} \left[ G(\mathbf{r}(\boldsymbol{\xi}_i); \mathbf{r}'(\boldsymbol{\xi}'_j)) + G(\mathbf{r}(\boldsymbol{\xi}'_i); \mathbf{r}'(\boldsymbol{\xi}_j)) \right], \tag{4}$$

where $\boldsymbol{\xi}_1 = (1/6, 1/6)$, $\boldsymbol{\xi}_2 = (2/3, 1/6)$, $\boldsymbol{\xi}_3 = (1/6, 2/3)$, $\boldsymbol{\xi}'_1 = (0, 1/2)$, $\boldsymbol{\xi}'_2 = (1/2, 0)$, and $\boldsymbol{\xi}'_3 = (1/2, 1/2)$ are the Gaussian quadrature points. Note that $\mathbf{r}(\boldsymbol{\xi}) = \mathbf{r}^1 H^1 + \mathbf{r}^2 H^2 + \mathbf{r}^3 H^3$, where $\mathbf{r}^1$, $\mathbf{r}^2$, and $\mathbf{r}^3$ are the three nodal location vector for the triangle, $H^1 = 1 - \xi - \eta$, $H^2 = \xi$, and $H^3 = \eta$ are the shape functions for the standard linear triangles, and $\boldsymbol{\xi} = (\xi, \eta)$ is the isoparametric coordinate for the standard linear triangles.

We note that if a Gaussian quadrature of degree 1 is used instead in the integration of the Eq. 3 for the case when $i \neq j$, a well-known formula for the mutual inductance of the two loops of wire at the centroid of the filamentary elements is obtained. Thus, the expression for filamentary mutual inductances in Eq. 3 reduces to that of the previous filamentary models in Ref. 4 and 5. Thus, the filamentary mutual inductance calculation approach discussed here is simply a generalization of the mutual inductance calculations of the past filamentary models. The present approach has an advantage of being able to integrate the quadruple integral in Eq. 3 to any arbitrary precision if desired. In practice, approximating the quadruple integral with a Gaussian quadrature of degree 2 has an advantage of removing a singular point in the integrand, thus allowing the same equation to be applied to the calculation of both the self and the mutual inductances.

### B. External Circuit

In theory, the externally applied voltage, $V^\alpha(t)$, in the Eq. 1 can be any arbitrary function of time, and any arbitrary external circuit model can be coupled with the filamentary circuit equation. However, for this implementation, ideal crowbar circuit is assumed for external circuits connected to the driver coils. The liner is assumed to have no external circuit connected to it.

The ideal crowbar circuit is composed of three circuit sections: capacitor bank, crowbar, and driver coil sections. The three sections contain a capacitor, diode, and driver coil, respectively, and has stray resistance and inductance associated with it. The ideal crowbar circuit behaves as a simple RLC circuit until the voltage across the driver coil section becomes negative. At this point, the current begins to flow through the crowbar section, which allows the current through the driver coil section to decay with a crowbar resistive time scale. The circuit diagram of the ideal crowbar circuit is given in Fig. 1.

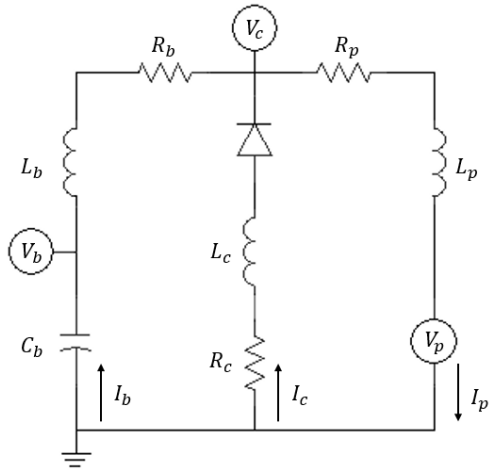


**Figure 1. Circuit diagram of the ideal crowbar circuit used in the model.**

In the ideal crowbar circuit, there are six unknowns, which corresponds to driver coil voltage ($V_p$) and current ($I_p$), capacitor bank voltage ($V_b$) and current ($I_b$), and crowbar section voltage ($V_c$) and current ($I_c$). Using Kirchhoff's circuit laws, following six circuit equations can be derived for the six unknowns:

$$I_p = \sum_i I_i^p, \tag{5}$$

$$V_c = R_p I_p + L_p \frac{dI_p}{dt} + V_p, \tag{6}$$

$$V_b = R_b I_b + L_b \frac{dI_b}{dt} + V_c, \tag{7}$$

$$I_b = -C_b \frac{dV_b}{dt}, \tag{8}$$

$$I_p = I_b + I_c, \tag{9}$$

and

$$I_c = 0 \tag{10a}$$

$$V_c = I_c R_c + L_c \frac{dI_c}{dt}. \tag{10b}$$

In the Eq. 10, the first form is used if the voltage across the crowbar section is positive, and the latter form is used if the voltage across the crowbar section is negative. In the equations, $I_i^p$ is the filamentary currents of the driver coil connected to the external circuit, $R_p$ and $L_p$ are the stray resistance and inductance of the driver section, respectively, $R_b$ and $L_b$ is the stray resistance and inductance of the capacitor bank section, respectively, $C_b$ is the capacitance of the capacitor bank, and $R_c$ and $L_c$ is the stray resistance and inductance of the crowbar section, respectively. The circuit equations for all external circuits can be coupled with the filamentary circuit equation and solve it simultaneously to obtain the time evolution of all circuit unknowns in the filamentary and external circuit system.

### C. Filamentary Thermal Equations

At the present time, the simplest locally adiabatic thermal model is used to model the heating of the coils due to Joule heating. Under the locally adiabatic assumption, each filaments is assumed to be adiabatic, and the effects of thermal conduction across filaments are neglected. While the locally adiabatic assumption is incorrect for long time scale phenomenas, since the thermal conduction time is generally a few orders of magnitude greater than the current penetration time scale, as long as the pulse length is short, the locally adiabatic assumption should yield accurate result. For example, if one considers commonly used coil and liner material, copper, the thermal diffusivity is of order $10^4\,\mathrm{mm}^2/\mu\mathrm{s}$, while the magnetic diffusivity is of order $10^2\,\mathrm{mm}^2/\mu\mathrm{s}$. Since typical liner implosion time scale is less than $10^2\,\mu\mathrm{s}$, it can be seen that the thermal conduction is negligible.

The locally adiabatic assumption allows for very simple and decoupled thermal advance equation given to be

$$\Delta T_i = \frac{R_i I_i^2}{c_{sp} m_i} \Delta t, \tag{11}$$

where $T_i$ is the temperature of the $i$-th filament, $c_{sp}$ is the specific heat, and $m_i$ is the mass of the $i$-th filament. While the use of temperature dependent specific heat is possible, at the current time, constant specific heat is assumed for simplicity. Once the filamentary temperature is given, the filament resistivity is advanced as function of time to be

$$\rho_i = \rho_{ref} \left[1 + \alpha_r (T_i - T_{ref})\right], \tag{12}$$

where $\rho_i$ is the resistivity of the $i$-th filament, $\rho_{ref}$ and $T_{ref}$ are the reference resistivity and temperature of the material, respectively, and $\alpha_r$ is the temperature coefficient for resistivity. At the present time, the thermo-mechanical effects are neglected, making filament resistivity and resistance the only variable that depends on the temperature.

### D. Structural Dynamics

In the past filamentary models of Miura and that of Novac, a constant volume assumption was made for the structural dynamics, which simplified the filamentary dynamics of the liner significantly.[4,5] The constant volume assumption was largely justified by the negligible time the liner spends in an elastic regime, allowing for simple volume conserving deformation in the plastic regime. Novac was able to extend the original model of the Miura and Nakao to include the effect of the axial dependence of the radial liner deformation through the use of filamentary row dynamics, but the model could not fully characterize the axial deformation of the liner, and the axial load contributions were neglected.[6]

In order to resolve both radial and axial deformation of the liner, a fully 2-Dimensional structural mechanics with large deformation theory is required. Due to the significant deformation that the liner experiences in the azimuthal direction during implosion, typical infinitesimal strain theory is unsuitable for characterizing liner dynamics. For this reason, a triangular finite element approach for large strain axisymmetric solids developed by Castelló and Flores is used along with the filamentary circuit equations.[7] For this model, the

liner material model is assumed to be isotropic with isochoric rate-independent $J_2$ plasticity. The thermo-mechanical coupling is also neglected in the material model. With these assumptions, the deformation gradient $\mathbf{F}$ is multiplicatively decomposed into an elastic part $\mathbf{F}^e$ and a plastic part $\mathbf{F}^p$. Due to the isochoric assumption, the plastic part does not modify the volume. Thus, the structural problem can be advanced as a two step process of an elastic predictor and a plastic corrector, which is equivalent to the original problem.

In the subsequent subsections, the methods of Castelló and Flores, which has been adapted for the filamentary model, are outlined. Majority of the steps outlined here follows closely to that in Ref. 7, with minor modifications made to simplify it for the assumptions in the filamentary model.

### 1. *Deformation Dynamics*

For this filamentary model, the updated Lagrangian approach of Castelló and Flores is used.[7] In this approach, the inverse of the elastic finger tensor, $\mathbf{b^{-1}} = \mathbf{F^{-T}F^{-1}}$, is defined as an internal variable characterizing the deformation of the system. In an updated Lagrangian approach, the system condition at the previous time step (previous material state) is assumed to be fully known. Thus, based on the deformation of the system relative to the previous material state, the inverse of the relative deformation gradient can be defined to be

$$\mathbf{f}_{n+1}^{-1} = \frac{\partial \mathbf{x}_n}{\partial \mathbf{x}_{n+1}} = \mathbf{F}_n \mathbf{F}_{n+1}^{-1}, \tag{13}$$

where $\mathbf{f}_{n+1}^{-1}$ is the inverse of the relative deformation gradient at the present configuration, $\mathbf{x}$ is material points, and subscripts $n$ and $n+1$ denotes previous and present configuration, respectively.

Knowing the inverse of the relative deformation gradient at the present configuration and the inverse of the elastic finger tensor at the previous time step, an updated inverse of the elastic finger tensor for the elastic predictor at the present time step can be computed to be

$$\mathbf{b}_{pre}^{-1} = \mathbf{f}_{n+1}^{-T} \mathbf{b}_n^{-1} \mathbf{f}_{n+1}^{-1}, \tag{14}$$

and the corresponding predicted Euler-Almansi strain tensor ($\mathbf{e}_{pre}$) is obtained to be

$$\mathbf{e}_{pre} = \frac{1}{2}(\mathbf{1} - \mathbf{b}_{pre}^{-1}), \tag{15}$$

where $\mathbf{1}$ is the identity tensor.

Since the plastic deformation is assumed to be isochoric, the hydrostatic pressure contribution to the Kirchhoff stress tensor can be evaluated at this point to be

$$p = -K \operatorname{tr}[\mathbf{e}_{pre}], \tag{16}$$

where $p$ is the hydrostatic pressure (assumed to be positive in compression) and $K$ is bulk modulus. The deviatoric stress is dependent on the plasticity to ensure that it lies within the $J_2$ yield surface, thus predictor-corrector approach has to be taken.

Assuming bilinear isotropic hardening material model, a very simple radial return algorithm can be applied to the deviatoric stress from the elastic predictor to obtain corrected stress. The predicted deviatoric Kirchhoff stress tensor ($\mathbf{s}_{pre}$) can be computed to be

$$\mathbf{s}_{pre} = -\mu \left\{ \mathbf{b}_{pre}^{-1} - \frac{\mathbf{1}}{3} \operatorname{tr}[\mathbf{b}_{pre}^{-1}] \right\}, \tag{17}$$

where $\mu$ is the shear modulus. From predicted deviatoric stress tensor, an effective trial stress ($s_{eff}$) can be computed to be

$$s_{eff} = \sqrt{\frac{3}{2} \mathbf{s}_{pre} : \mathbf{s}_{pre}}. \tag{18}$$

If the effective trial stress is below the yield stress from the previous configuration, then the response is elastic, and the plastic correction can be skipped. However, if the effective trial stress surpasses the yield stress, then using the radial return algorithm, the incremental plastic strain ($\Delta\epsilon^p$) can be calculated to be

$$\Delta\epsilon^p = \frac{s_{eff} + \sigma_y^n}{3\mu + E_t}, \tag{19}$$

where $\sigma_y^n$ is yield stress at the previous configuration and $E_t$ is tangent modulus. The total plastic strain is tracked internally, and it is incremented with the result from Eq. 19. From the incremental plastic strain, the plastic correction factor ($\alpha_p$) can be obtained to be

$$\alpha_p = 1 - \frac{3\mu\Delta\epsilon^p}{s_{eff}}, \tag{20}$$

and the corrected deviatoric Kirchhoff stress tensor is obtained to be

$$\mathbf{s}_{n+1} = \alpha_p \mathbf{s}_{pre}. \tag{21}$$

In order to ensure that there is a consistent strain state that matches the corrected stress state, the elastic Finger tensor must also be updated with the radial return algorithm. Since the plasticity only affects the deviatoric stress which is proportional to the deviatoric part of the elastic Finger tensor, the non-deviatoric part of the elastic Finger tensor is invariant under the plastic deformation. Thus, using the definition of the predicted and corrected deviatoric Kirchhoff stress tensor, the inverse of a corrected elastic Finger tensor can be calculated to be

$$\mathbf{b}_{n+1}^{-1} = \alpha_p \mathbf{b}_{pre}^{-1} + \mathbf{1}\frac{1-\alpha_p}{3}\mathrm{tr}[\mathbf{b}_{pre}^{-1}] \tag{22}$$

The updated inverse of the elastic Finger tensor for this time step can be used in next time step to continue to advance the liner structural dynamics.

Using the corrected deviatoric Kirchhoff stress tensor, the total corrected Kirchhoff stress for this time step can be obtained to be

$$\boldsymbol{\tau}_{n+1} = \mathbf{s}_{n+1} - p\mathbf{1} \tag{23}$$

and from a weak form of the momentum equation for the Updated Lagrangian approach, the expression for internal work is obtained to be

$$\delta W_{int} = \int \delta\epsilon : \tau \, dV_{n+1} \tag{24}$$

where $W_{int}$ is work due to internal deformation and $\epsilon$ is infinitesimal strain tensor. From the internal work, nodal forces can be calculated to advance the nodal position to the new configuration. The whole procedure outline in this section can be completed, given the inverse of the relative deformation gradient (used in Eq. 14) and the variation of the infinitesimal strain tensor (used in Eq. 24) for the current configuration. Thus, the goal of the finite element approximation is to relate the nodal positions to these two quantities.

### *2. Finite Element Approximation*

For the filamentary model, 3-node triangular elements are used to discretize the problem domain. Again, we follow the approaches of Castelló and Flores, and we form a patch of four triangle (one which is central, and three neighboring triangles) to obtain quadratic interpolation for the strain calculations over the triangular patch.[7] The quadratic shape function ($\mathbf{N}^l$) is defined to be

$$\mathbf{N}^l = \begin{bmatrix} N^1 \\ N^2 \\ N^3 \\ N^4 \\ N^5 \\ N^6 \end{bmatrix} = \begin{bmatrix} \zeta + \xi\eta \\ \xi + \eta\zeta \\ \eta + \zeta\xi \\ \frac{1}{2}\zeta(\zeta-1) \\ \frac{1}{2}\xi(\xi-1) \\ \frac{1}{2}\eta(\eta-1) \end{bmatrix}, \tag{25}$$

where $\xi$, $\eta$, and $\zeta = 1 - \xi - \eta$ are the local coordinates for the triangular patch. Similar nodal index convention as the Castelló and Flores is used, except with the axial direction on the primary axis and the radial direction on the secondary axis.

In the axisymmetric geometry, the component of the relative deformation gradient inverse is given to be

$$\mathbf{f}_{n+1}^{-1} = \begin{bmatrix} \frac{\partial z_n}{\partial z_{n+1}} & \frac{\partial z_n}{\partial r_{n+1}} & 0 \\ \frac{\partial r_n}{\partial z_{n+1}} & \frac{\partial r_n}{\partial r_{n+1}} & 0 \\ 0 & 0 & \frac{r_n}{r_{n+1}} \end{bmatrix} = \left[\begin{array}{c|c} \mathbf{f}^{-1} & \mathbf{0} \\ \hline \mathbf{0} & \lambda^{-1} \end{array}\right]. \tag{26}$$

In Eq. 26, it can be seen that the azimuthal contribution is just a diagonal term, which is the azimuthal stretch. The in-plane (rz-plane) contribution is simply the inverse of the 2-D relative deformation gradient. Thus, we split the two contribution into in-plane and out-of-plane component and define the in-plane component $\mathbf{f}^{-1}$ and the out-of-plane component $\lambda^{-1}$.

Using the finite element decomposed triangular patch with its shape function, $\mathbf{x} = \sum_{l=1}^{6} N^l \mathbf{x}^l$ where $\mathbf{x} = [z, r]$, the relative deformation gradient inverses can be expressed in terms of nodal values. After application of chain rule, the in-plane relative deformation gradient inverse becomes

$$\mathbf{f}^{-1} = \sum_{l=1}^{6} \frac{\partial N^l}{\partial \boldsymbol{\xi}} \left( \sum_{m=1}^{6} \frac{\partial N^m}{\partial \boldsymbol{\xi}} \mathbf{x}_{n+1}^m \right)^{-1} \mathbf{x}_n^l = \sum_{l=1}^{6} N_{,\mathbf{x}}^l(\boldsymbol{\xi})\, \mathbf{x}_n^l, \tag{27}$$

where $\boldsymbol{\xi} = [\xi, \eta]$ and $N_{,\mathbf{x}}^l(\boldsymbol{\xi})$ is defined to be the in-plane local relative gradient coefficients. Since for standard 3-node triangles, strains are constant over the element, we want to reduce the non-constant strain for the 5-node triangle patch to constant through averaging. To accomplish this, we follow the approach of Castelló and Flores and take the radially weighted average of the relative deformation gradient inverse at the center of the neighboring triangle edges.[7] Thus, the patch averaged relative deformation gradient inverse ($\bar{\mathbf{f}}^{-1}$) is obtained to be

$$\bar{\mathbf{f}}^{-1} = \sum_{l=1}^{6} \frac{\sum_{i=1}^{3} N_{,\mathbf{x}}^l(\boldsymbol{\xi}_i) r(\boldsymbol{\xi}_i)}{\sum_{i=1}^{3} r(\boldsymbol{\xi}_i)} \mathbf{x}_n^l = \sum_{l=1}^{6} \bar{N}_{,\mathbf{x}}^l \mathbf{x}_n^l, \tag{28}$$

where $\bar{N}_{,\mathbf{x}}^l$ is defined to be the in-plane relative gradient coefficients.

Similar to the in-plane component, patch averaged ratio of the relative azimuthal stretch inverse must be calculated for the out-of-plane component. Again, we follow the approach of Castelló and Flores and compute the azimuthal stretch inverse at the center of the four 3-node triangle element that makes up the triangle patch and take the weighted average of the four values. We use weighting of 3-to-1 for the center and off-center triangle values, as suggested by Castelló and Flores.[7] We obtain the patch averaged azimuthal stretch inverse to be

$$\bar{\lambda}^{-1} = \frac{1}{6} \left\{ 3 \sum_{l=1}^{3} \left( \frac{1}{\sum_{m=1}^{3} r_{n+1}^l} r_n^l \right) + \sum_{K=1}^{3} \left[ \sum_{l_K=1}^{3} \left( \frac{1}{\sum_{m_K=1}^{3} r_{n+1}^{m_K}} r_{n+1}^{l_K} \right) \right] \right\} = \sum_{l=1}^{6} \bar{M}^l r_n^l, \tag{29}$$

where the index $K$ corresponds to the three 3-node triangle element adjacent to the central triangle, and the indices $m_K$ and $l_K$ corresponds to the local node index of the adjacent 3-node triangle element $K$. The coefficient $\bar{M}^l$ is defined to be the out-of-plane relative gradient coefficients, and can be found by simplifying the weighted average.

For the case when the central triangle is on the boundary, and it has neighboring triangles missing, a ghost node approach suggest by Castelló and Flores is used for the in-plane component, and for the out-of-plane component, the contribution is neglected and the weighting is adjusted accordingly.[7] With the boundary triangles properly accounted, Eq. 28 and Eq. 29 can be used to define an averaged relative deformation gradient inverse, which can be used in Eq. 14 to compute the updated inverse of the elastic finger tensor. Eq. 15 to 23 can then be calculated for the current configuration.

To obtain the variation of the infinitesimal strain required for Eq. 24, we note that the infinitesimal strain is defined in an axisymmetric system as

$$\epsilon = \frac{1}{2}[(\nabla_{n+1}\mathbf{u})^T + \nabla_{n+1}\mathbf{u}] = \begin{bmatrix} \frac{\partial u_z}{\partial z_{n+1}} & \frac{1}{2}\left( \frac{\partial u_z}{\partial r_{n+1}} + \frac{\partial u_r}{\partial z_{n+1}} \right) & 0 \\ \frac{1}{2}\left( \frac{\partial u_z}{\partial r_{n+1}} + \frac{\partial u_r}{\partial z_{n+1}} \right) & \frac{\partial u_r}{\partial r_{n+1}} & 0 \\ 0 & 0 & \frac{u_r}{r_{n+1}} \end{bmatrix}, \tag{30}$$

where $\mathbf{u} = [u_z, u_r]$ is the displacement vector in the axial and radial direction. Similar procedure as the relative deformation gradient inverse can be carried out for the infinitesimal strain by noting that $\mathbf{u} = \sum_{l=1}^{6} N^l \mathbf{u}^l$ and applying chain rule. Using same average procedure as the relative deformation gradient inverse, the variation of the infinitesimal strain can be defined in terms of previously define coefficients as

$$\delta \begin{bmatrix} \epsilon_{zz} \\ \epsilon_{rr} \\ 2\epsilon_{rz} \\ \epsilon_{\phi\phi} \end{bmatrix} = \sum_{l=1}^{6} \begin{bmatrix} \bar{N}_{,z}^l & 0 \\ 0 & \bar{N}_{,r}^l \\ \bar{N}_{,r}^l & \bar{N}_{,z}^l \\ 0 & \bar{M}^l \end{bmatrix} \begin{bmatrix} \delta u_z^l \\ \delta u_r^l \end{bmatrix}. \tag{31}$$

The Eq. 31 can then be used in Eq. 24 to obtain nodal forces and advance the nodal position to the next time step.

### *3. Nodal Force Integration and Explicit Advance*

For this filamentary model, an explicit time stepping method with lumped sum nodal mass (diagonal mass matrix) is used to advance the nodal position to the next time step. To diagonalize the mass matrix, the filamentary element mass is partitioned to its nodes as

$$m^l = 2\pi \int \rho_m r H^l dr dz \tag{32}$$

where $m^l$ is the mass at $l$-th node, $\rho_m$ is mass density, $H^l$ is the $l$-th shape function, and the integral is evaluated over the filamentary element cross-section.

In principle, various approaches can be taken to account for magnetic forces at each nodes produced from the current distribution computed from the filamentary circuit equations (Eq. 1). For this model, the magnetic force on the filamentary element is approximated by the volume integrated $J \times B$ force, and the nodal forces are computed from the decomposition of elemental forces. To obtain magnetic fields due to filamentary currents, we use magnetic vector potential for axisymmetric cylindrical problems, given to be

$$A_\phi(r,z) = \frac{\mu_0}{4\pi r} \iint J_\phi(r',z') G(r,z;r',z') dr' dz',$$

which for filamentary models with constant current densities over each filaments reduces to

$$A_\phi(\mathbf{r}) = \frac{\mu_0}{4\pi r} \sum_{\alpha=1}^{N_p} \sum_{j=1}^{N_e^\alpha} \frac{I_j^\alpha}{S_j^\alpha} \int_{\Omega_j^\alpha} G(\mathbf{r};\mathbf{r}')\, dr' dz', \tag{33}$$

where $\Omega_j^\alpha$ is the 2-D cross-sectional domain of the $j$-th filamentary elements on the $\alpha$-th coil. Using Eq. 33 and the definition of the magnetic vector potential ($\mathbf{B} = \nabla \times \mathbf{A}$), the magnetic field at point $(r,z)$ can be expressed in terms of Green's function to be

$$\mathbf{B}(r,z) = \frac{\mu_0}{4\pi r} \sum_{\alpha=1}^{N_p} \sum_{j=1}^{N_e^\alpha} \frac{I_j^\alpha}{S_j^\alpha} \iint_{\Omega_j^\alpha} \left( -\hat{\mathbf{r}} \frac{\partial G}{\partial z} + \hat{\mathbf{z}} \frac{\partial G}{\partial r} \right) dr' dz', \tag{34}$$

where $N_p$ is number of current carrying coils, $N_e^\alpha$ is number of filamentary elements in the $\alpha$-th coil, $I_j^\alpha$ is the current flowing through the $j$-th filament in the $\alpha$-th coil, and $S_j^\alpha$ is the cross-sectional area of the $j$-th filament in the $\alpha$-th coil. The two spatial derivatives of the Green's functions are obtained analytically to be

$$\frac{\partial G}{\partial z} = \frac{(z-z')k}{2\sqrt{rr'}(1-k^2)} \left[ 2(1-k^2)K(k) - (2-k^2)E(k) \right]$$

and

$$\frac{\partial G}{\partial r} = \frac{k}{2(1-k^2)} \sqrt{\frac{r}{r'}} \left\{ 2(1-k^2)K(k) - \left[ 2 - \left( 1 + \frac{r'}{r} \right) k^2 \right] E(k) \right\}.$$

Using the form of the magnetic field in Eq. 34, the total magnetic force acting on the $i$-th filamentary element ($\mathbf{F}_i$) can be computed to be

$$\mathbf{F}_i = \frac{\mu_0 I_i}{S_i} \int_{\Omega_i} \mathbf{I}_B(r,z)\, dr dz, \tag{35}$$

where $\mathbf{I}_B$ is the effective current vector, defined to be

$$\mathbf{I}_B(r,z) = \frac{1}{2} \sum_{\alpha=1}^{N_p} \sum_{j=1}^{N_e^\alpha} \frac{I_j^\alpha}{S_j^\alpha} \int_{\Omega_j^\alpha} \left( \hat{\mathbf{r}} \frac{\partial G}{\partial r} + \hat{\mathbf{z}} \frac{\partial G}{\partial z} \right) dr' dz'. \tag{36}$$

We see that the magnetic force on the $i$-th liner filament is proportional to its self current times the area average of the effective current vector. To simplify the evaluation of the magnetic force, we approximate the

area average of the effective current vector as the average of the effective current vector at the filamentary element nodes. The partitioning of the elemental force to the nodal force can also be simplified by assuming equal force contribution from all three nodes. Under these simplifying assumptions, the nodal force contribution due to $i$-th filamentary element can be computed to be $\mathbf{F}_i/3$.

To obtain nodal force from the internal forces, we use Eq. 31 with Eq. 24. To obtain nodal force from the variation in internal work, we apply common technique from principle of virtual work to isolate virtual displacement for each nodes. We isolate the contribution to each nodes by setting virtual displacements of all other nodes equal to zero, except for itself. Under this virtual displacement condition, the internal work is related to nodal forces as

$$\delta W_{int} = -(f_z^l \delta u_z^l + f_r^l \delta u_r^l), \tag{37}$$

where $f_z^l$ and $f_r^l$ is the nodal force in $z$ and $r$ direction, respectively, for the $l$-th node. Thus, the nodal force can be computed to be

$$\begin{bmatrix} f_z^l \\ f_r^l \end{bmatrix} = -2\pi \iint \begin{bmatrix} \tau_{zz}\bar{N}_{,z}^l + \tau_{zr}\bar{N}_{,r}^l \\ \tau_{rr}\bar{N}_{,r}^l + \tau_{zr}\bar{N}_{,z}^l + \tau_{\phi\phi}M^l \end{bmatrix} r\, drdz. \tag{38}$$

Since both the deformation gradient coefficients and the Kirchhoff stresses are constant over the four triangle patch, it can be pulled out of the integral, thus simplifying the internal force calculations.

Once the magnetic and the internal nodal forces are computed for all nodes, the velocity and the position of the nodes can be updated using Newton's 2nd law. Since the mass matrix is diagonalized and lumped sum mass is given at each nodes, each nodes can be advanced independently as non-interacting particles, saving the computational cost of the nodal advance at each time step.

### E. Numerical Method

In this implementation of the filamentary model, the filamentary circuit, thermal, and structural equations discussed in the previous sections are solved sequentially at each time step to advance the driver and liner system to the next time step. The code was implemented in modern Fortran using object-oriented approaches. The flowchart of the implement filamentary model is given in Fig. 2. The present implementation does not use sophisticated time step control between the three physics solvers (circuit, thermal, and structural), thus sufficiently small time step must be chosen by the user to ensure stability.

For the coupled filamentary and external circuit equations, an implicit advance of the currents and voltages are used with non-linear terms related with filamentary circuit parameters (time dependent resistance and inductance for filaments) linearized. The non-linear terms in the filamentary circuit parameters are removed through the use of a single Picard iteration with the values at the next time step predicted from that of the current and the previous time level. The dense matrix system of equations are then solved using LU factorization method using LAPACK routines DGETRF and DGETRS.

Both the thermal and the structural advances are handled using explicit forward Euler method. For the structural advance, after the relevant internal and external forces are calculated, explicit forward Euler time stepping is used for the velocity and position advance. Due to the explicit nature of the time stepping, if the time step is too large, the solution can go unstable. The required time step is usually smaller than what is predicted by the typical Courant-Friedrichs-Lewy conditions for structural mechanics based on the material sound speed, since for most cases, the instabilities develops due to the inability for the internal force correction to keep up with the perturbation caused by the externally applied magnetic force. As a simple remedy, the velocity and position advance for the internal and the magnetic forces are split into three step process, where the internal force advance is split into two half steps which is applied before and after the magnetic force advance. From numerical experiments, this seems to offer slightly better stabilization compared with a single velocity and position advance, but a sufficiently small time step still has to be used.

While the explicit time stepping in the thermal and structural advances places stringent constraint on the size of the time step, its explicit nature fully decouples the systems of equations in these two physics, allowing easy parallelization of these embarrassingly parallel regions. Taking advantage of this decoupled nature of the explicit advance significantly improves the performance of the code in a multi-core shared memory architecture. However, due to the dense matrix inversion that is required for the advance of the circuit equations, the performance is limited by the efficiency of the dense matrix solver.

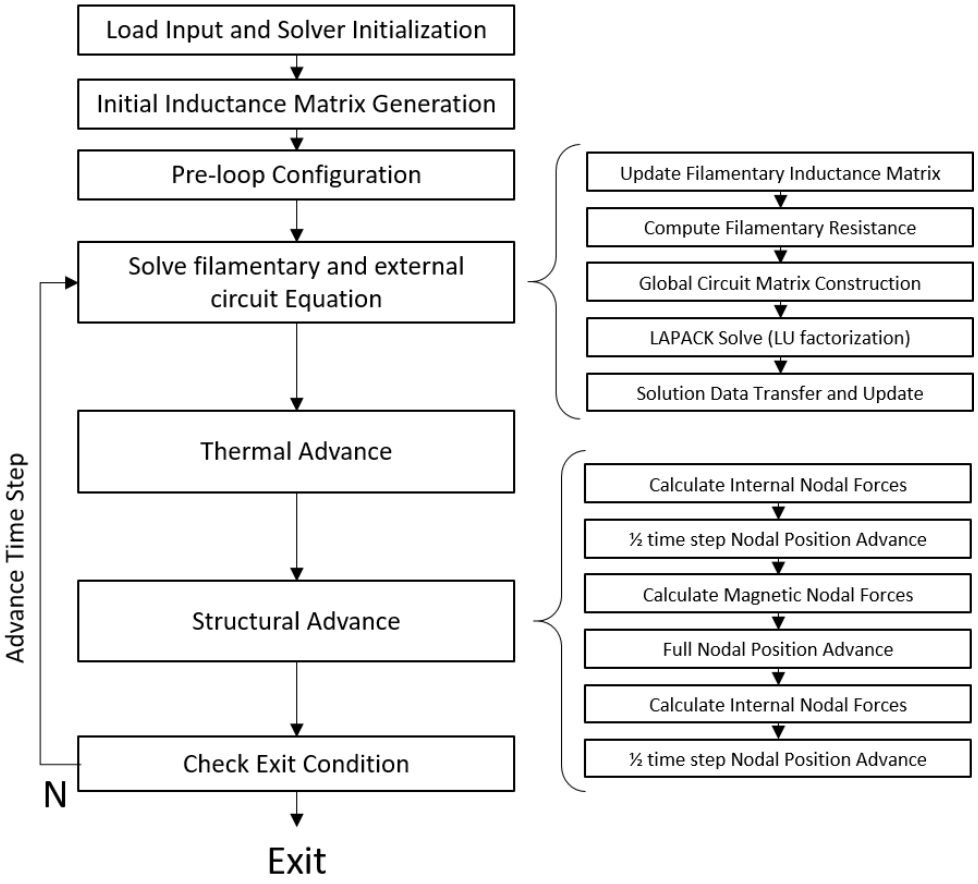


**Figure 2. Flowchart of the filamentary model presented.**

## III. Preliminary Results from the Filamentary Model

In this section, preliminary results from the simulation of an electromagnetic inductive drive using the filamentary model is given. A simple liner implosion calculation is set up for this purpose using a single driver coil and a single liner. No bias coils are included in the system; thus, the effect of an initial seed bias flux is neglected. The geometry of the driver and liner system is chosen based on dimensions that are possible to test in the MSNW facilities. The circuit values are chosen based on past experiences performing inductively driven liner implosion experiments at MSNW and Plasma Dynamics Lab (PDL) at University of Washington.[8] The details of the simulation setup is given in subsection A, and the results are discussed in subsection B. Finally in subsection C a comparison is made with the previous pseudo-1D liner model to assess the difference of the present model compared with the past liner model for the characterization of the liner implosion.

### A. Analysis Setup

For the simplified electromagnetic inductive drive model, a driver coil inner radius of 6 cm is assumed, which represents an approximate size of a driver coil that can be tested in the MSNW facilities. From this driver coil radius, the outer radius of the liner is fixed to 5.5 cm. From the past pseudo-1D model, reducing the gap between the inner radius of the driver coil and the outer radius of the liner was beneficial in increasing the efficiency of the energy transfer from the stored bank energy to the liner kinetic energy. However, from past experiences, some clearance is required for electrical insulation and vacuum boundary. Thus, a clearance of 5 mm is given between the driver and the liner to accommodate these requirements.

For the FRC confinement and capture, relatively long liner is desired to capture typical elongated FRCs that are produced from the formation process. For this reason, a liner length of 10.5 cm is chosen to

accommodate the capture of a FRC with elongation of at least one. The driver coil length is set to 10 cm, which is slightly smaller than the liner. According to past liner studies, this is expected to reduce the effect of barrel distortion due to end effects.[4] A liner thickness of 1 mm is chosen based on the previous pseudo-1D liner results.[3] Both the liner and the driver is assumed to be made from aluminum, which were the materials that were used in the past liner implosion experiments conducted at PDL.[8] The geometry configuration for the liner and the driver are summarized in Table 1. A 720 kJ driver bank charged to 30 kV is assumed for the driver circuit. A negligible stray inductance and resistance of 1 nH and 1 mΩ is assumed for the bank and the crowbar leg of the ideal crowbar circuit.

The values of the material properties used for aluminum is given in Table 2. A linear elastic bilinear hardening model is assumed for liner. The hardening of the aluminum is cut-off at the ultimate stress to stop hardening phenomena at higher internal stress levels. The resistivity and mass densities are an initial values. The resistivity is updated as function of temperature using the temperature coefficient. Initial temperature of 300 K is assumed for both the driver coil and the liner. The mass density is updated based on the nodal dynamics, as a fixed mass is associated with the node at the beginning of the solver process. To simplify the calculation, the driver is assumed to be rigid in the model, while the liner is allowed to be deformable.

| **Inputs** | **Driver** | **Liner** |
|---|---|---|
| Inner Radius | 6 cm | 5.4 cm |
| Outer Radius | 7 cm | 5.5 cm |
| Length | 10 cm | 10.5 cm |
| Material | Aluminum | Aluminum |
| Circuit | Crowbar | None |

**Table 1. Summary of the driver coil and the liner configuration.**

| **Property** | **Value** |
|---|---|
| Mass Density | $2.7\,\mathrm{g/cm^3}$ |
| Young's Modulus | 69 GPa |
| Poisson's Ratio | 0.3 |

| **Property** | **Value** |
|---|---|
| Tangent Modulus | 2 GPa |
| Yield Strength | 200 MPa |
| Ult. Strength | 600 MPa |

| **Property** | **Value** |
|---|---|
| Specific Heat | $900\,\mathrm{J/kg\,m\,K}$ |
| Resistivity | $2.65 \times 10^{-8}\,\Omega\,\mathrm{m}$ |
| Temp. Coeff. | $3.9 \times 10^{-3}\,\mathrm{K^{-1}}$ |

**Table 2. Summary of aluminum material properties used for this analysis.**

The driver and the liner is meshed with 3-node triangular elements. In order to ensure that the inductances calculated for each filamentary triangle elements using Eq. 4 gives sufficient accuracy and stability in the circuit equation, the aspect ratio of the triangle is controlled. The minimum and the maximum element edge length for the driver is kept to 0.5 mm and 1.5 mm, respectively. The maximum aspect ratio for the driver mesh is 1.9. The minimum and the maximum element edge length for the liner is kept to 0.25 mm and 1.4 mm, respectively. The maximum aspect ratio for the liner mesh is 2.7. The initial mesh for the driver and the liner is given in Fig. 3.

### B. Summary of Results

The resulting filamentary code result for the driver and liner system described in the previous subsection shown in Fig. 4 to 8. The Fig. 4 contains the resulting time dependent global circuit results for the driver and the liner filamentary circuits. As expected for the ideal crowbar circuit, the driver voltage drops slightly below zero and slowly decays back down to zero voltage as the crowbar circuit prolongs the current flowing in the driver. Since stray resistances and inductances are set to low values, negligible oscillation and overshoot is seen in the voltage and current in the driver circuit. For the liner current, the expected reverse current that forms due to Lenz's law is seen, as the liner current follows driver current closely in the reverse direction. The sharp decay and positive reversal of the liner current near the end of the implosion is also a characteristic behavior for the liner as the magnetic flux of the driver coil that bled through the liner is compressed by the implosion of the liner. Thus, the filamentary circuit results shows expected behavior for the electromagnetic inductive implosion of the liner that was seen in the past with the pseudo-1D liner code.

The Fig. 5 contains the resulting radial position and velocity time history data for the liner. The slow start at the initial launch of the liner is caused by the inertia of the liner, and its behavior agrees with what was observed in the past with the pseudo-1D liner code.[3] The Fig. 6 shows the implosion of the liner at the selected time together with the magnetic flux contours. As it can be seen from Fig. 6, barrel distortion is controlled by the increase of liner length, and the ends lags behind rest of the liner. Due to the lagging

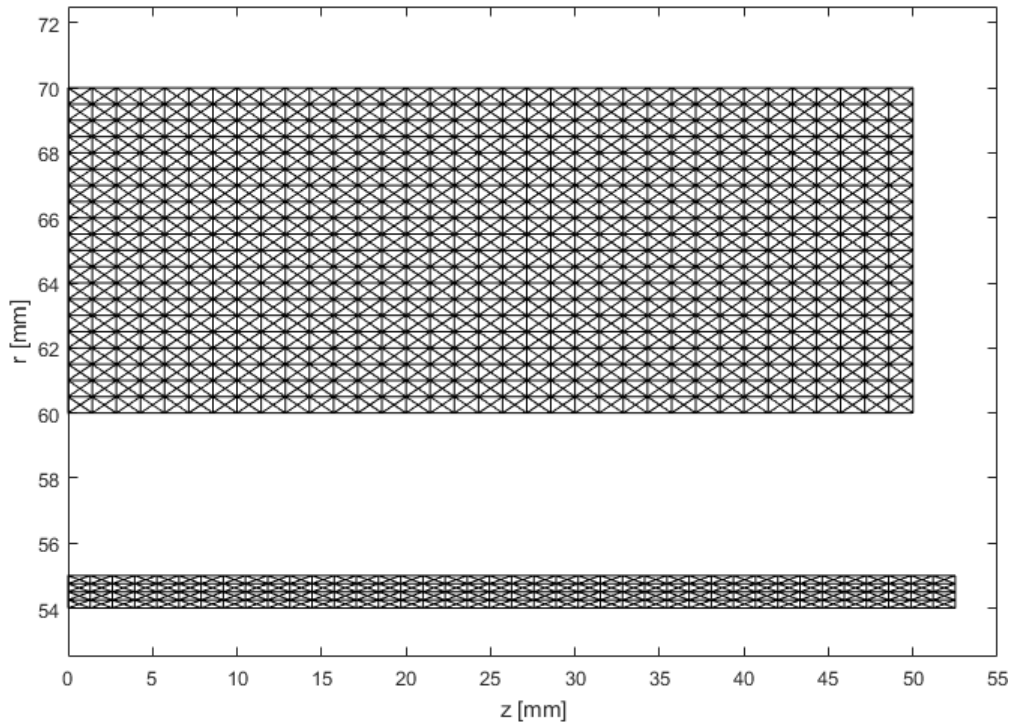


**Figure 3. The initial mesh of the driver and the liner. A symmetric mesh is used and only half of the problem domain is shown in the figure for clarity.**

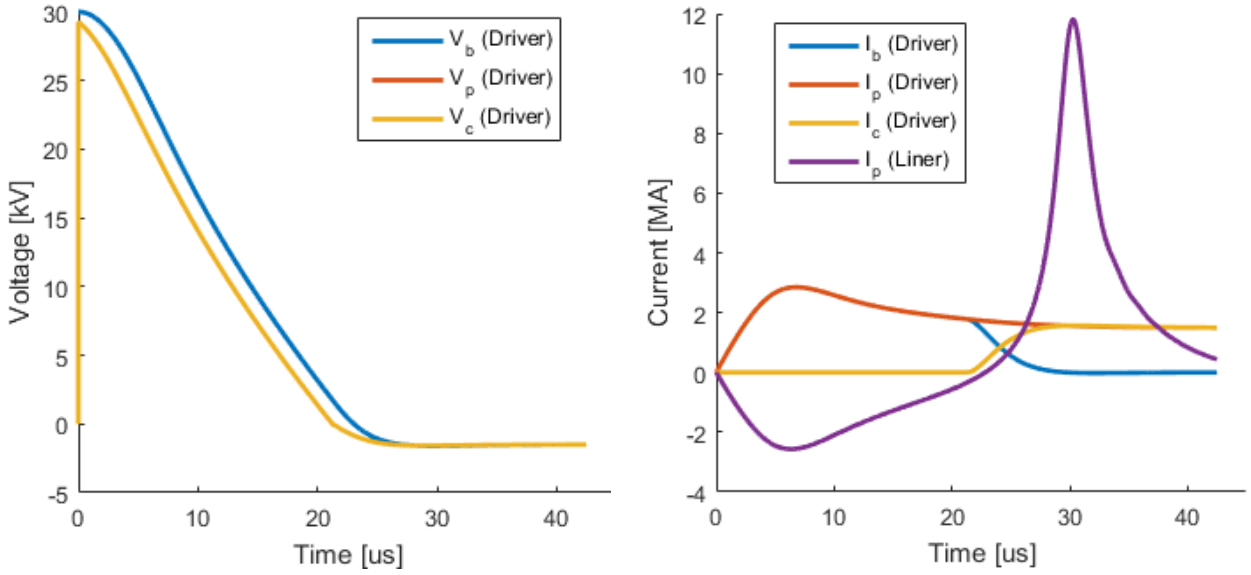


(a) Time history of the driver circuit voltage

(b) Time history of the driver circuit and liner current

**Figure 4. Time history of the driver and liner circuit quantities. The driver circuit values are for the ideal crowbar circuit.**

effect of the ends, the liner shows significant thickening in the radial position plot in Fig. 5, which is due to the reversed barrel distortion rather than natural thickening of the liner due to plastic volume conservation. This time dependent evolution of the liner distortion can be more clearly seen in Fig. 8.

The expected turn-around behavior of the liner implosion is seen in the results of 5. When the liner turns around, the inner surface first stops, while the remaining of the structure is still imploding radially.

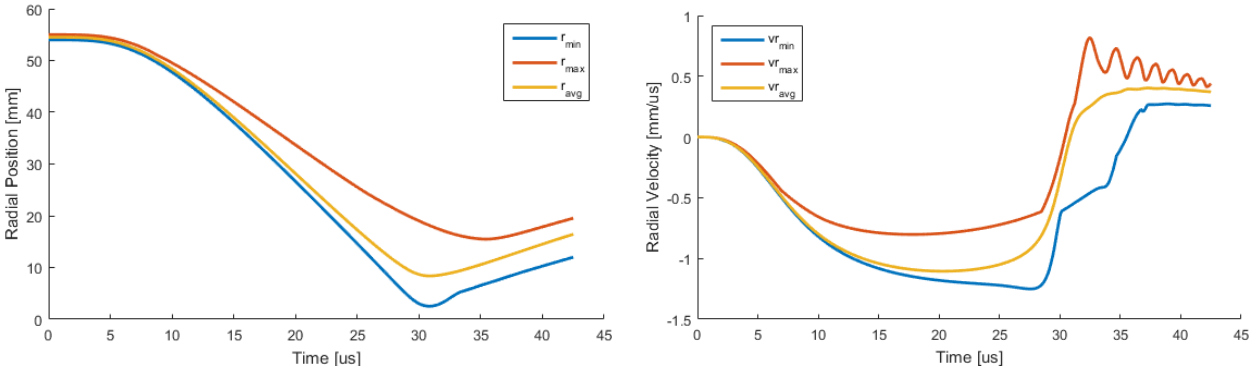


(a) Time history of liner radial position

(b) Time history of liner radial velocity

**Figure 5. Time history of the liner radial position and velocity calculated from the filamentary code. The Minimum, maximum, and average of the nodal values are given.**

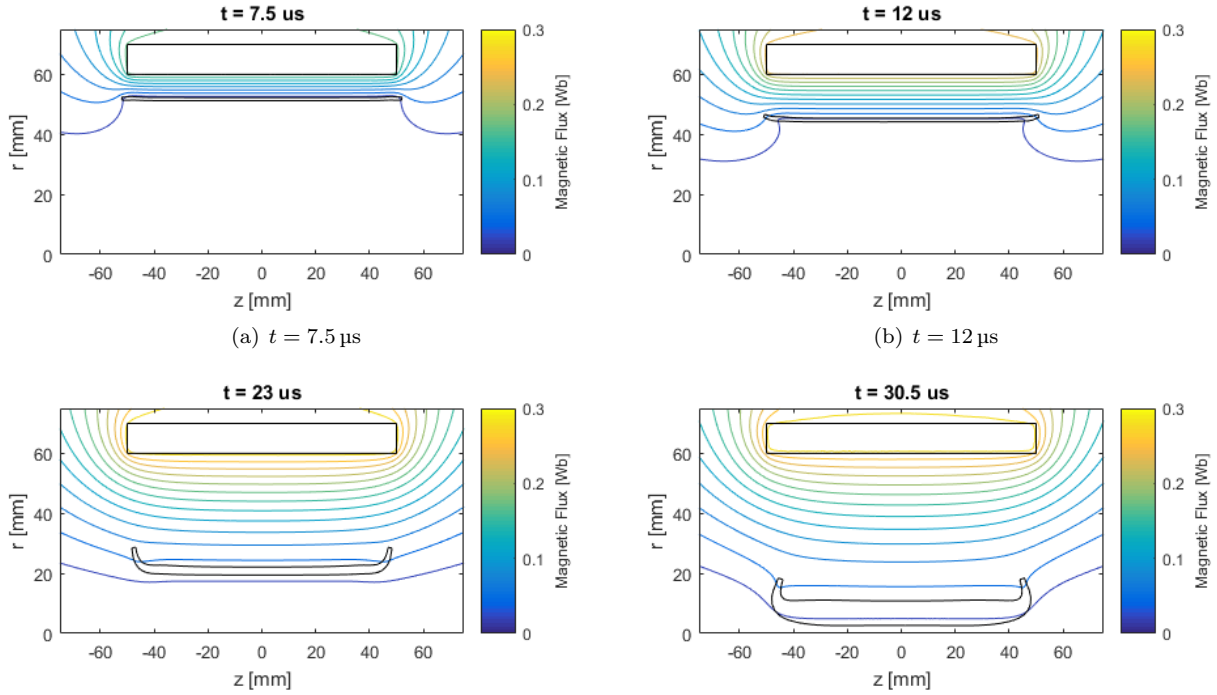


(a) $t = 7.5\,\mu s$

(b) $t = 12\,\mu s$

(c) $t = 23\,\mu s$

(d) $t = 30.5\,\mu s$

**Figure 6. Magnetic flux contours for the driver and liner system at selected times.**

There is a turn-around lag time due to the finite time it takes for the pressure wave from the inner surface of the liner to reach the remainder of the liner. The ends experience significantly delayed turn-around due to its lagging distortion. The expected kinetic energy loss at the turn-around is seen as the magnitude of the reversed velocity of the liner is lower than the imploding velocity. The oscillation of the maximum velocity in 5 is caused due to the bending oscillation of the distorted ends. The peak magnetic field magnitude profile at the liner turn-around is shown in Fig. 7. A field magnitude of 350 T is obtained, which is within the expected magnitude of the obtainable flux compression with the inductive methods. In general, the results obtained from the filamentary code seems to reproduce expected behaviors of the liner.

In the magnetic flux results shown in Fig. 6, a visible magnetic flux diffusion is present due to finite resistivity of the liner. Due to the temperature dependent resistivity of the liner and the driver, the flux penetration through the ends are enhanced, reducing the adverse edge current effect that can cause barrel distortion. Due to the liner length being too long in this calculation, the lagging distortion is produced. Since

no bias flux is using in the present calculation, there is no correcting magnetic force from inside the liner that helps reduce the radial distortion of the liner. Thus, the liner continue to exhibit lagging behavior at the end during the entire implosion process, as the internal forces tries to maintain plastic volume conservation.

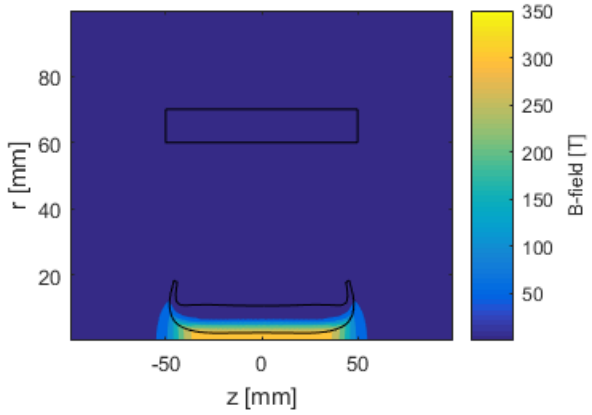


**Figure 7. The magnetic field magnitude profile at the liner turn-around.**

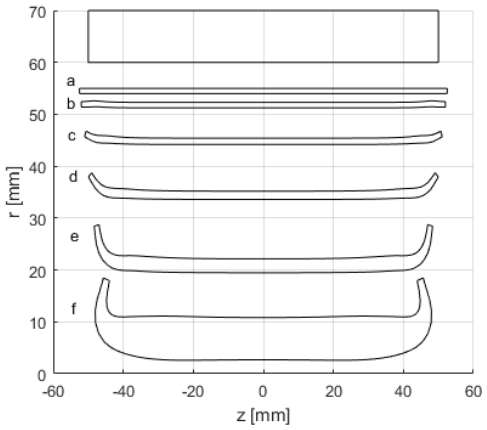


**Figure 8. Deformation of the liner at various times after the driver bank fire: a.** $t = 0\,\mu s$**; b.** $t = 7.5\,\mu s$**; c.** $t = 12\,\mu s$**; d.** $t = 17\,\mu s$**; e.** $t = 23\,\mu s$**; and f.** $t = 30.5\,\mu s$**.**

Compared with past liner calculations of Miura and that of Novac, the end lag distortion obtained in this analysis is significantly larger than what is expected.[4,5] Furthermore, the end lag distortion seems more aggressive than what was suggested by the past liner implosion experiment at PDL.[8] More test cases using various sweep of the liner length is required to characterize the effect of the end distortion phenomena, but one possible explanation for this behavior is the lack of initial seed flux. If a seed flux is present inside the liner, there is stabilizing magnetic tension force from inside the liner, which will oppose the radial distortion of the liners ends.

Another possibility is a 3-D effect which is missing in the 2-D axisymmetric structural dynamic assumptions. In the past 3-D ANSYS Structural Explicit Dynamics calculations using assumed electromagnetic loading pressure on the liner surfaces, development of azimuthal buckling was observed for imploding liners.[9] From the ANSYS calculations, it was seen that the azimuthal buckling pattern that develops in the liner has a stabilizing effect on the radial distortion, as it increases the stiffness of the liner to radial bending.[3] To account for the azimuthal structural dynamics more accurately without writing a fully 3-D code, an isotropic material model may need to be modified to include an anisotropic effect in the azimuthal direction in the current model. These are areas that additional improvements can be made to the model in the future to better recover the expected liner behaviors.

### C. Comparison with Past 1D Liner Code

To assess the importance of the 2-dimensional effects and the accuracy of the pseudo-1D model, a test case that has a similar configuration as the case that was ran with the filamentary code is ran in a pseudo-1D liner code described in Ref. 3. The results from the pseudo-1D liner code is plotted over the filamentary code result for the liner radial position and the circuit currents, and is shown in Fig. 9. Based on the circuit results, the pseudo-1D liner code predicts a faster quarter-cycle time compared with the filamentary code. This can be caused by two factors. One possibility is that the driver-liner system inductance computed from the two code disagrees and the pseudo-1D liner code predicts a smaller system inductance compared with the filamentary model. This will case change to the L/R time constant for the circuit, which can explain change in the quarter cycle time. Second possibility is that the filamentary model is more dissipative than the pseudo-1D model so the quarter cycle time is being modified by the resistive effect. Since the peak current obtained in the filamentary model is lower than that of the pseudo-1D model, the second possibility is more likely. However, both cases will have to be considered to identify the reason for disagreement.

Since the implosion is more rapid with higher peak current, more kinetic energy is transfered to the liner in the pseudo-1D liner code. This effect can be seen in the slightly faster liner implosion time in the Fig. 9 and more aggressive current decay in the driver circuit. As a result, the pseudo-1D liner code predicts liner

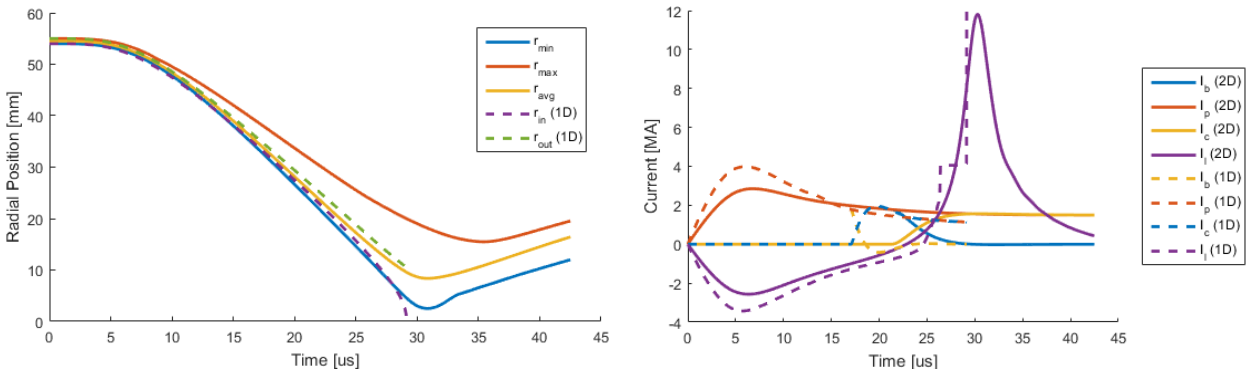


(a) Time history of the liner radial position

(b) Time history of the driver and liner current

**Figure 9. Comparison between filamentary code and the pseudo-1D liner code for the time history of the driver and liner radial position and current. The data for the filamentary code is shown in solid lines and the pseudo-1D liner code is shown in dashed lines.**

kinetic energy transfer of 30.4 %. On the other hand, the filamentary code predicts slower liner implosion and slower decay of the driver current. Thus, the initial capacitive energy stored in the bank is dissipated by the resistive losses and stored in a magnetic field as an inductive energy. With the filamentary model, a kinetic energy transfer of only 8.3 %. In the past pseudo-1D liner code studies, the optimization of the kinetic energy transfer was strongly dependent on the initial driver current profile in the acceleration phase of the liner.[3] Thus, the disagreement between the two codes stems mostly from the difference in the peak current and the quarter cycle time. Re-evaluating the inductance and resistance calculation in both the pseudo-1D liner code and the filamentary code may be necessary to resolve the disagreement between the two codes.

## IV. Conclusion

An axisymmetric and fully 2-dimensional filamentary model for the electromagnetic inductive driver for a liner implosion fusion thruster system was developed and implemented in this study. The sequential coupling of the filamentary circuit model with the axisymmetric 2-D large strain finite element model seems to work well to characterize the liner implosion behavior in the inductive drive as long as the time step is kept small. In the future, the use of a predictor-corrector loop may allow for a larger time stepping to improve solver performance and improve stability.

Preliminary results suggest some disagreements with the previous pseudo-1D liner model and suggests presence of a significantly more resistive energy dissipation than what was seen before in the past studies. A further testing and development is necessary to identify the source of the disagreement and improve the implemented filamentary model. In particular, the inductance and resistance calculation in the present and the previous model need a careful review to ensure time dependent circuit behavior agrees with each other when the liner deformation is small. To control the radial distortion in the liner, a more detailed consideration of the azimuthal direction may be necessary to account for the azimuthal buckling stiffening effect. In the future, these issues must be considered to further improve the model for the electromagnetic inductive drive.

## Appendix A: Derivation of Filamentary Circuit Equation for Deformable Solids

In this Appendix, we derive a filamentary circuit equations for deformable solids in axisymmetric configuration. We first start with a resistive generalized Ohm's law, given to be

$$\mathbf{E} = \rho\mathbf{J} - \mathbf{v} \times \mathbf{B} \tag{A.1}$$

where $\mathbf{E} = -\nabla\varphi - \partial\mathbf{A}/\partial t$ is the electric field, $\varphi$ is the electrostatic potential, $\mathbf{A}$ is the magnetic vector potential, $\rho$ is the resistivity, $\mathbf{J}$ is current density, $\mathbf{v}$ is local velocity of the deformable solid, and $\mathbf{B}$ is the magnetic field. Using axisymmetric assumption for the magnetic field and the current, only the azimuthal

component of the Eq. A.1 is non-trivial, and after some simplification, it is given to be

$$\frac{DA_\phi}{Dt} = -\frac{1}{r}\frac{\partial \varphi}{\partial \phi} - \rho J_\phi - \frac{v_r}{r} A_\phi \tag{A.2}$$

where $D/Dt$ is the Lagrangian or the material derivative. Integrating Eq. A.2 over the volume of the $i$-th filament at the $n$-th time configuration, we obtain an integral form of the Eq. A.2 at time step $n$ to be

$$-\int_{\Omega_i^n} \frac{\partial \varphi_i}{\partial \phi}\, d\Omega_i^n = \int_{\Omega_i^n} \frac{DA_\phi}{Dt} r\, d\Omega_i^n + \int_{\Omega_i^n} \rho J_\phi r\, d\Omega_i^n + \int_{\Omega_i^n} v_r A_\phi\, d\Omega_i^n \tag{A.3}$$

where in the above expression, the azimuthal integration has already been carried out and $\Omega_i^n$ represents 2-dimensional region in the $rz$-plane for the $i$-th filament at time step $n$.

At this point, we note that the expression for magnetic vector potential for axisymmetric cylindrical magnetostatics problem is given to be

$$A_\phi(r,z) = \frac{\mu_0}{4\pi r} \iint J_\phi(r',z') G(r,z;r',z') dr' dz' \tag{A.4}$$

where $A_\phi$ is magnetic vector potential, $\mu_0$ is permeability of free space, $J_\phi$ is azimuthal current density, and $G(r,z;r'z')$ is a Green's function defined as

$$G(r,z;r'z') = \sqrt{(r+r')^2 + (z-z')^2}\left[(2-k^2)K(k) - 2E(k)\right]$$

where $K(k)$ and $E(k)$ are the complete elliptic integral of the first and second kind, respectively, and the modulus $k$ is defined to be

$$k^2 = \frac{4rr'}{(r+r')^2 + (z-z')^2}$$

Now, we can use the filamentary assumption of constant azimuthal current density across each filamentary element and the super position principle. Assuming that all of the current carrying elements in the entire problem domain is composed of filamentary elements, the Eq. A.4 simplifies to

$$A_\phi(\mathbf{r}) = \frac{\mu_0}{4\pi r} \sum_j \frac{I_j^n}{S_j^n} \int_{\Omega_j^n} G(\mathbf{r};\mathbf{r}_j)\, d\Omega_j^n \tag{A.5}$$

where $I_j^n$ is the current flowing through the $j$-th filament at time step $n$ and $S_j^n$ is the cross-sectional area of the $j$-th filament at time step $n$. Combining Eq. A.5 with Eq. A.3 and simplifying, we obtain

$$\begin{aligned} -\frac{2\pi}{S_i^n}\int_{\Omega_i^n} \frac{\partial \varphi_i}{\partial \phi}\, d\Omega_i^n =& \frac{1}{S_i^n}\frac{D}{Dt}\left[\sum_j S_i^n I_j \frac{\mu_0}{2S_i^n S_j^n}\int_{\Omega_i^n}\int_{\Omega_j^n} G(\mathbf{r}_i;\mathbf{r}_j)\, d\Omega_j^n d\Omega_i^n\right] + \frac{2\pi I_i^n}{(S_i^n)^2}\int_{\Omega_i^n} \rho r\, d\Omega_i^n \\ &+ \sum_j I_j \frac{\mu_0}{2S_i^n S_j^n}\int_{\Omega_i^n}\int_{\Omega_j^n} \frac{v_r}{r} G(\mathbf{r}_i;\mathbf{r}_j)\, d\Omega_j^n d\Omega_i^n \end{aligned} \tag{A.6}$$

We now associate various terms in the Eq. A.6 to typical circuit quantities. The term on the left is related with the voltage drop across the filament which is caused by externally applied voltages. Assuming constant voltage across the cross-section of the filament, it reduces to the familiar voltage drop term in the circuit equation. We can also immediately see that the second term on the right hand side is a resistive contribution. Assuming constant resistivity across the cross-section of the filament, the expression reduces to a familiar equation for the resistance of the circular current carrying elements, given to be

$$R_i^n = \frac{2\pi \bar{r}_i^n \rho}{S_i^n} \tag{A.7}$$

where $\bar{r}_i^n$ is the mean radius of the $i$-th filamentary element at $n$-th time step.

The first and the last term on the right hand side of Eq. A.6 is related with a mutual inductance term. To see this, we note that given two filamentary elements $i$ and $j$, the magnetic energy between the two filaments ($W_{ij}$) are given to be

$$W_{ij} = \frac{1}{2}\int \mathbf{J}_i \bullet \mathbf{A}_j\, d^3x \tag{A.8}$$

where $\mathbf{J}_i$ is current density of the $i$-th filament and $\mathbf{A}_j$ is magnetic vector potential due to filament $j$. The volume integral is taken over the volume of the $i$-th filament. For two filaments, Eq. A.8 can also be expressed equivalently in terms of mutual inductance as

$$W_{ij} = \frac{1}{2} M_{ij} I_i I_j \tag{A.9}$$

where $M_{ij}$ is the mutual inductance between filaments $i$ and $j$, and $I_i$ and $I_j$ are the total current flowing through the $i$-th and the $j$-th filament, respectively. It can be seen that combining Eq. A.8 and Eq. A.9 yields equations for mutual inductance in terms of magnetic vector potential. We now note that for the filamentary model, a constant azimuthal current density is assumed over the filamentary element. Using this assumption and a form of a magnetic vector potential given in Eq. A.4, an expression for the mutual inductance between filamentary element $i$ and $j$ can be obtained to be

$$M_{ij}^n = \frac{\mu_0}{2} \frac{1}{S_i^n S_j^n} \int_{\Omega_i^n} \int_{\Omega_j^n} G(\mathbf{r}_i; \mathbf{r}_j)\, d\Omega_j^n d\Omega_i^n \tag{A.10}$$

We see that the mutual inductance of the two filamentary elements is simply proportional to the area averages of the Green's function over the two filaments. Thus, we obtain a form for the mutual inductance between the two filaments, which closely resembles the terms in Eq. A.6. To simplify Eq. A.6, we make an assumption that $v_r/r$ is constant over the filaments, so this term can be pulled out of the integral and the mutual inductance term can be isolated. We then obtain

$$\Delta\varphi_i^n = \sum_j \frac{d}{dt}\left(M_{ij}^n I_j^n\right) + R_i^n I_i^n + \frac{1}{\mathcal{V}_i^n} \frac{d\mathcal{V}_i^n}{dt} \sum_j M_{ij}^n I_j^n \tag{A.11}$$

where $\Delta\varphi_i^n$ is voltage drop across the $i$-th filament at $n$-th time step and $\mathcal{V}_i^n$ is the volume of the $i$-th filament at $n$-th time step. Thus, a familiar filamentary circuit equation derived by Miura and Nakao (Ref 4) is obtained with one additional term related with a volume change of the filamentary elements. Thus, for deformable filaments, one additional volume dependent contribution must be included. For the case of metal liners, since the liner spends majority of its time in plastic regime during implosion where the volume of the liner is conserved, the last term of Eq. A.11 is negligible.

## References


[1]Slough, J., Pancotti, A., Kirtley, D., and Votroubek, G., "Electromagnetically Driven Fusion Propulsion," *33rd International Electric Propulsion Conference*, October 2013.

[2]Pancotti, A., Slough, J., and Shimazu, A., "Mars Mission Trade Studies and Technology Development of a 36 MW Fusion Rocket," *Joint Conference of 30th International Symposium on Space Technology and Science, 34th International Electric Propulsion Conference, and 6th Nano-satellite Symposium*, July 2015.

[3]Shimazu, A., Slough, J., and Pancotti, A., "Parametric Optimization of the Fusion Driven Rocket Liner Compression Driver," *52nd AIAA/SAE/ASEE Joint Propulsion Conference, AIAA Propulsion and Energy Forum*, July 2016.

[4]Miura, N. and Nakao, K., "Computer Analysis of Megagauss Field Generation by Condenser Bank Discharge," *Japanese Journal of Applied Physics*, Vol. 29, No. 8, 1990, pp. 1580–1599.

[5]Novac, B. M., Smith, I. R., and Hubbard, M., "2-D Modeling of Electromagnetic Flux-Compression in $\theta$-Pinch Geometry," *IEEE Transactions on Plasma Science*, Vol. 32, No. 5, 2004, pp. 1896–1901.

[6]Novac, B. M. and Smith, I. R., "Advances in the Filamentary Modelling of Electromagnetic Flux Compression," *Japanese Journal of Applied Physics*, Vol. 45, No. 4A, 2006, pp. 2807–2811.

[7]Castelló, W. B. and Flores, F. G., "A Triangular Finite Element with Local Remeshing for the Large Strain Analysis of Axisymmetric Solids," *Computer Methods in Applied Mechanics and Engineering*, Vol. 198, No. 2, 2008, pp. 332–343.

[8]Slough, J., Pancotti, A., and Shimazu, A., "The Fusion Driven Rocket: Nuclear Propulsion through Direct Conversion of Fusion Energy (Phase 2 Final Report) - NASA Grant: NNX12AR39G," 2015.

[9]Slough, J., Pancotti, A., and Kirtley, D., "Analysis of inductively driven liners for the generation of megagauss magnetic fields," *Magnetic Field Generation and Related Topics (MEGAGUSS), 2012 14th International Conference on Megagauss*, Oct 2012.